

# Quantum tunneling high-speed nano-excitonic modulator

Received: 30 May 2024

Accepted: 23 September 2024

Published online: 09 October 2024



Hyeonwoo Lee<sup>1,7</sup>, Sujeong Kim<sup>1,7</sup>, Seonhye Eom<sup>2</sup>, Gangseon Ji<sup>2</sup>, Soo Ho Choi<sup>3</sup>, Huitae Joo<sup>1</sup>, Jinhyuk Bae<sup>1</sup>, Ki Kang Kim<sup>3,4</sup>, Vasily Kravtsov<sup>5</sup>, Hyeon-Ryeol Park<sup>1,2</sup> & Kyoung-Duck Park<sup>1,6</sup> ✉

High-speed electrical control of nano-optoelectronic properties in two-dimensional semiconductors is a building block for the development of excitonic devices, allowing the seamless integration of nano-electronics and -photonics. Here, we demonstrate a high-speed electrical modulation of nanoscale exciton behaviors in a MoS<sub>2</sub> monolayer at room temperature through a quantum tunneling nanoplasmonic cavity. Electrical control of tunneling electrons between Au tip and MoS<sub>2</sub> monolayer facilitates the dynamic switching of neutral exciton- and trion-dominant states at the nanoscale. Through tip-induced spectroscopic analysis, we locally characterize the modified recombination dynamics, resulting in a significant change in the photoluminescence quantum yield. Furthermore, by obtaining a time-resolved second-order correlation function, we demonstrate that this electrically-driven nanoscale exciton-trion interconversion achieves a modulation frequency of up to 8 MHz. Our approach provides a versatile platform for dynamically manipulating nano-optoelectronic properties in the form of transformable excitonic quasiparticles, including valley polarization, recombination, and transport dynamics.

Excitons significantly influence the optical and electrical characteristics of two-dimensional semiconductors, with their distinct excitonic properties and strong light-matter interactions<sup>1</sup>. This contributes to the development of a range of exciton-based devices, enabling high-efficiency photodetectors<sup>2</sup>, light-emitting diodes<sup>3</sup>, excitonic lasers<sup>4,5</sup>, and photovoltaic elements<sup>6</sup>. On the other hand, the distinct excitonic properties of different excitonic quasiparticles, such as trions, dark excitons, and localized excitons, further expand the potential scope of applications. For example, the prolonged coherence time of dark excitons and the single-photon emitting behaviors of localized excitons have stimulated the potential applications for the exploration of Bose-Einstein condensation in semiconductors<sup>7–9</sup> and the generation of quantum light<sup>10–12</sup>, respectively. Likewise, given the characteristics

of trions, particularly the sensitivity to the external electric field<sup>13,14</sup> and the slow spin-flip process<sup>15,16</sup>, trions provide a breakthrough approach for the practical exciton transport and valleytronic applications. In addition, the modified recombination dynamics of trions greatly influences the photoluminescence (PL) quantum yield (QY)<sup>17</sup>, facilitating the development of the high-efficiency field-effect transistor and light-harvesting devices<sup>18–20</sup>.

Recently, exciton-to-trion conversion and trion-to-exciton conversion have been actively investigated, because the associated change in intrinsic parameters, including spin splitting, radiative decay rate, binding energy, and transport characteristics, can serve as control knobs for tailoring optoelectronic properties of materials<sup>13,15,21–23</sup>. While various techniques, such as chemical treatment<sup>24</sup>, photo-induced

<sup>1</sup>Department of Physics, Pohang University of Science and Technology (POSTECH), Pohang, Republic of Korea. <sup>2</sup>Department of Physics, Ulsan National Institute of Science and Technology (UNIST), Ulsan, Republic of Korea. <sup>3</sup>Center for Integrated Nanostructure Physics, Institute for Basic Science (IBS), Suwon, Republic of Korea. <sup>4</sup>Department of Energy Science, Sungkyunkwan University (SKKU), Suwon, Republic of Korea. <sup>5</sup>School of Physics and Engineering, ITMO University, Saint Petersburg, Russia. <sup>6</sup>Institute for Convergence Research and Education in Advanced Technology, Yonsei University, Seoul, Republic of Korea. <sup>7</sup>These authors contributed equally: Hyeonwoo Lee, Sujeong Kim. ✉e-mail: [parklab@postech.ac.kr](mailto:parklab@postech.ac.kr)

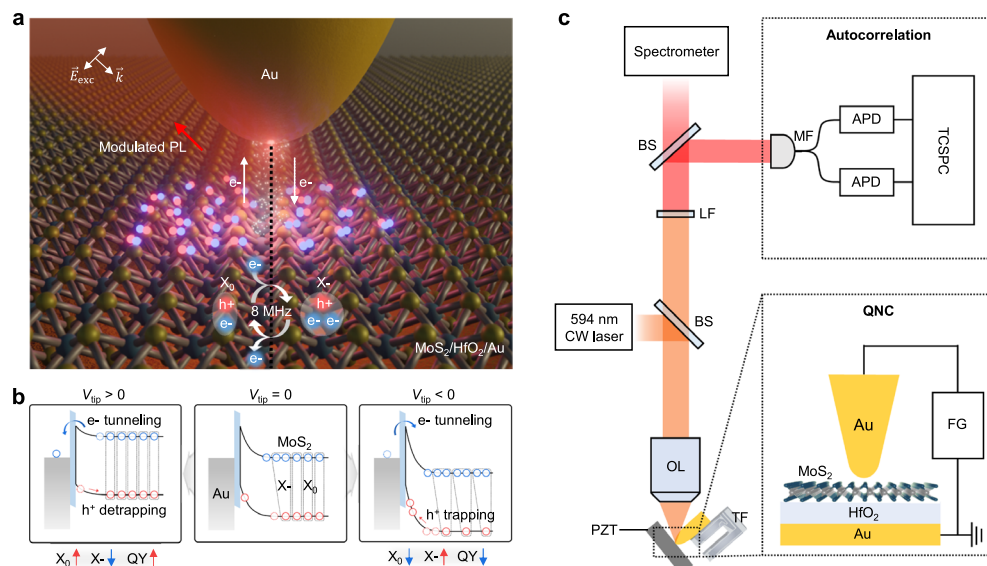


**Fig. 1 | Quantum tunneling nanoplasmonic cavity and high-speed exciton-trion interconversion.** **a** Illustration of high-speed trion-to-exciton (left) and exciton-to-trion (right) conversions within the QNC. Excitation light is projected with wave vector  $\vec{k}$  and its electric field  $\vec{E}_{\text{exc}}$ . **b** Band diagram of the MoS<sub>2</sub> ML in contact with the plasmonic Au tip under positive (top), zero (middle), and negative (bottom)  $V_{\text{tip}}$ . **c** Schematic of the QNC combined with the autocorrelation measurement

setup. Abbreviations: neutral-density filter (ND), half-wave plate ( $\lambda/2$ ), beam splitter (BS), objective lens (OL), tuning fork (TF), long-pass filter (LF), multimode fiber (MF), avalanche photodiode (APD), and function generator (FG), Lead zirconate titanate (PZT), quantum tunneling nanoplasmonic cavity (QNC), monolayer (ML), photoluminescence (PL), quantum yield (QY), time-correlated single-photon counting (TCSPC), neutral exciton (X<sub>0</sub>), trion (X<sup>-</sup>), electron (e<sup>-</sup>), hole (h<sup>+</sup>).

doping<sup>25</sup>, and plasmonic hot-electron injection<sup>26</sup>, have been extensively investigated, the electrostatic doping holds great potential for the seamless integration into industrial nano-electronic devices. Specifically, electrostatic doping stands out for its high-speed, non-destructive, reversible, and stable nature in modifying electron density, enabling versatile exciton-trion interconversion. However, the large-area electrical gating with the diffraction-limited optical analysis significantly diminishes the degree of integration and introduces potential delay factors impeding the speed of the device, restricting the integration of high-speed nano-electronics and -photonics.

Here, we demonstrate a high-speed electrical modulation of exciton-trion interconversion in a MoS<sub>2</sub> monolayer (ML) at room temperature. The use of a plasmonic Au tip and the MoS<sub>2</sub> ML results in formation of a quantum tunneling nanoplasmonic cavity (QNC), which enables nanoscale electrical control of tunneling electrons with simultaneously local probing of the correspondingly modified nano-optoelectronic responses with nano-localized optical field<sup>27</sup>. We achieve dynamic switching between neutral exciton (X<sub>0</sub>) dominant state and trion (X<sup>-</sup>) dominant state at the nanoscale region. This leads to a significant alteration in the radiative recombination rate, as evidenced by observed changes in the PL QY. By obtaining a second-order correlation function between two split PL signals with a time-correlated single-photon counting (TCSPC) system, we demonstrate the high-speed exciton-trion interconversion and correspondingly modified recombination dynamics with a modulation frequency of up to 8 MHz. Our finding presents a versatile platform for controlling the population of neutral excitons and trions at the nanoscale region, with high-speed electrical manipulation of nano-optoelectronic properties.

## Results

### Exciton-trion interconversion in QNC

Figure 1a illustrates the electrically controlled exciton-trion interconversion within the QNC. The distance between the Au tip and the MoS<sub>2</sub> ML is in the quantum tunneling range, accompanied by the formation of a dielectric barrier in a nanoscale gap<sup>28</sup>. Without the external bias on the Au tip ( $V_{\text{tip}}$ ), the coexistence of X<sub>0</sub> and X<sup>-</sup> is attributed to sulfur vacancies, defects, and trapped holes at the

interface of the MoS<sub>2</sub> ML<sup>29–31</sup>. Specifically, the trapping of photo-generated holes in MoS<sub>2</sub> ML increases electron density by leaving behind unpaired electrons in the conduction band, which act as free carriers<sup>32,33</sup>. Upon applying a positive  $V_{\text{tip}}$ , electrons in the conduction band of the MoS<sub>2</sub> ML migrate toward the Au tip while decreasing the density of trapped holes. This process results in a decreased X<sup>-</sup> density and an increased X<sub>0</sub> density, leading to a significantly enhanced PL QY<sup>17,22</sup>. By contrast, applying a negative  $V_{\text{tip}}$  causes electron tunneling from the Au tip to the conduction band of the MoS<sub>2</sub> ML with increasing the density of trapped holes. This process leads to an increased X<sup>-</sup> density with a decreased X<sub>0</sub> density, consequently deteriorating the PL QY<sup>17,22</sup>. Therefore, the electrical control of exciton-trion interconversion and its simultaneous nano-optical characterizations can be performed at the nanoscale region, as shown in Fig. 1b. Note that the  $V_{\text{tip}}$  indicates the experimentally applied voltage on the tip through the function generator (Supplementary Fig. 1).

To facilitate dynamic switching between the X<sub>0</sub> and X<sup>-</sup> dominant states in the QNC, we initially adjust the free carrier density of the MoS<sub>2</sub> ML without applying the  $V_{\text{tip}}$ . The MoS<sub>2</sub> ML is transferred onto a thin HfO<sub>2</sub> layer deposited on an Au substrate, which results in X<sup>-</sup> density comparable to X<sub>0</sub> density under ambient conditions, attributed to the oxygen vacancy formation at the interface between oxide-deficient high-k oxides and semiconductors<sup>34,35</sup> (Supplementary Fig. 2). Therefore, the following experiments are conducted with the MoS<sub>2</sub> ML on the HfO<sub>2</sub>/Au substrate. The HfO<sub>2</sub> layer thickness is optimized to achieve a comparable density between X<sub>0</sub> and X<sup>-</sup>, while simultaneously inhibiting direct electron transfer between the MoS<sub>2</sub> ML and the Au substrate, thereby minimizing Ohmic losses. By employing a shear-force atomic force microscopy (AFM) technique<sup>36–38</sup>, we approach the conductive Au tip to the MoS<sub>2</sub> ML rigidly within the quantum tunneling range, inducing nanoscale electrostatic doping. The highly confined optical field at the Au tip apex enables the sub-diffraction-limited probing of nano-optoelectronic properties within the QNC. In addition, we combine the TCSPC system for the autocorrelation measurement to confirm the high-speed electrical modulation of exciton-trion interconversion and correspondingly modified recombination dynamics in the MoS<sub>2</sub> ML, as shown in Fig. 1c (Methods).

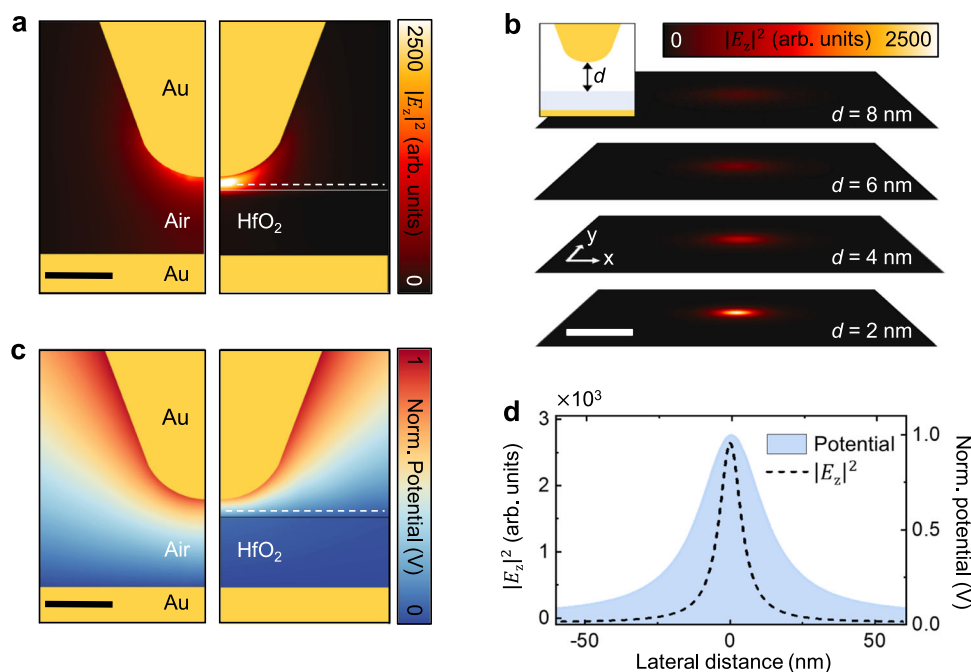


**Fig. 2 | Spatial distribution of optical field and electric potential in the quantum tunneling nanoplasmonic cavity.** **a** Distribution of the optical field intensity  $|E_z|^2$  without (left) and with (right) the  $\text{HfO}_2$  layer, when the tip- $\text{HfO}_2$  distance is 2 nm. **b**  $|E_z|^2$  distribution in a xy-plane for different tip- $\text{HfO}_2$  distances. The tip-sample distance is denoted as  $d$ . The z-position of cross-sectional view is fixed along the

white dashed line ( $\text{MoS}_2$  ML) in (a). **c** Distribution of the electric potential without (left) and with (right)  $\text{HfO}_2$  layer when  $d = 2$  nm, upon applying the DC bias on the tip. **d** Profile of optical field intensity  $|E_z|^2$  (black dashed line) and electric potential (blue filled region), derived from white dashed lines in (a) and (c).

### Pre-characterizations of QNC

We investigate the nanoscale confinement of the optical field and the electric potential in the quantum tunneling plasmonic cavity with finite-difference-time-domain and computer simulation technology methods, respectively. Figure 2a shows the highly localized optical field at the Au tip apex, attributed to localized surface plasmon resonance and lightning rod effects<sup>39,40</sup>. The presence of the  $\text{HfO}_2$  layer significantly enhances the optical field confinement due to the dipole-dipole interaction at the gap<sup>41–43</sup>. The optical field intensity and the spatial confinement dramatically increase with decreasing tip-sample distance  $d$ , as shown in Fig. 2b (Supplementary Fig. 3). In the quantum tunneling regime, specifically at  $d \leq 2$  nm, the highly confined optical field with a full-width at half-maximum of  $\sim 10$  nm is observed (Supplementary Fig. 4), which can induce nanoscale plasmon-exciton interaction in the  $\text{MoS}_2$  ML. Figure 2c shows the distribution of the electric potential with the application of  $V_{\text{tip}}$ , exhibiting the nanoscale dimension of the electric potential resulting from the nanoscale geometry of the metallic tip. This allows for precise nanoscale modulation of electrons and trapped holes at the metal-semiconductor interface, while effectively preventing the undesired release of localized holes at impurities or defects within the  $\text{MoS}_2$  ML<sup>32</sup>. Therefore, we demonstrate that the QNC facilitates nanoscale electrostatic doping and enables sub-diffraction-limited observation of nano-optoelectronic properties, as shown in Fig. 2d (Supplementary Fig. 5). We also confirm the reproducibility and stability of nanoscale exciton-trion interconversion (Supplementary Figs. 6–8).

### Optical and electrical control of exciton behaviors

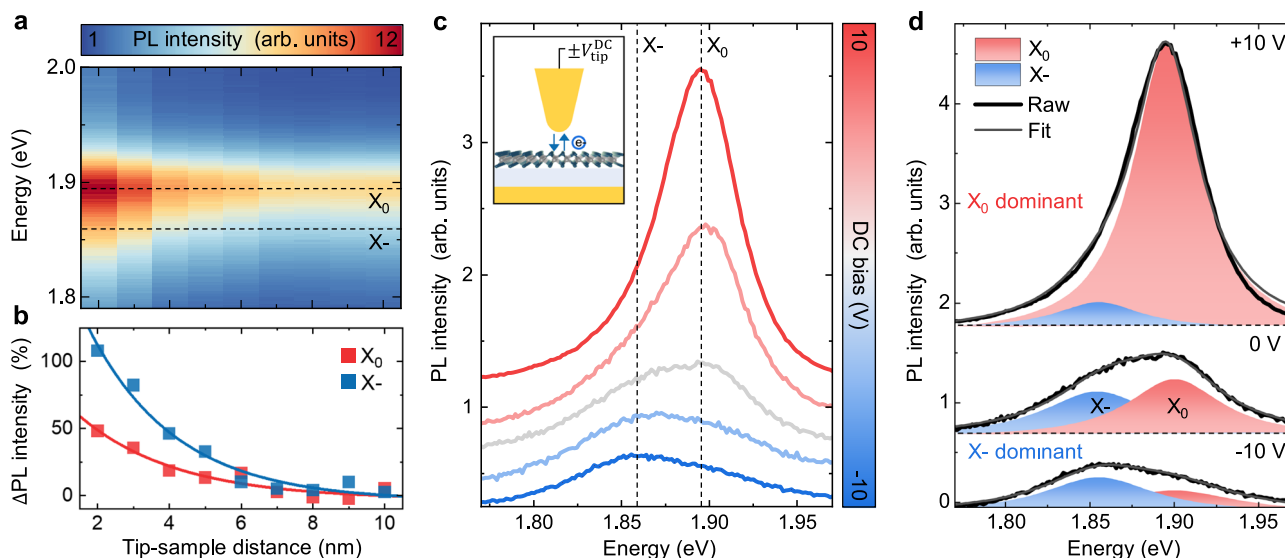
To experimentally investigate the effect of the modifying optical field confinement on the emission properties of the  $\text{MoS}_2$  ML, we observe the PL spectrum while systematically decreasing the tip-sample distance with  $< 0.1$  nm uncertainty. We reveal a noticeable enhancement in the  $X_0$  emission intensity, accompanied by the emergence of a peak at lower energy, which can be assigned to  $X^-$ <sup>44</sup>, as shown in Fig. 3a.

Figure 3b clearly demonstrates the rapidly increasing intensities of both  $X_0$  and  $X^-$  as the tip-sample distance decreases. The enhanced optical field with decreasing tip-sample distance leads to the increased  $X_0$  emission intensity, as demonstrated in Fig. 2a, b. The correspondingly increased  $X^-$  emission intensity can be attributed to the direct hot electron injection from the Au tip and the accumulation of trapped hole states (Supplementary Figs. 9, 10)<sup>31,45</sup>. These processes are induced and controlled by engineering the optical field strength underneath the Au tip. In addition, compared to the far-field, there are increases of  $\sim 49\%$  in  $X_0$  intensity and  $\sim 108\%$  in  $X^-$  intensity, indicating the dominant near-field signal compared to the far-field.

We then apply a DC bias on the Au tip ( $V_{\text{tip}}^{\text{DC}}$ ) to control the electron density of the  $\text{MoS}_2$  ML within the quantum tunneling nanoplasmonic cavity, as shown in Fig. 3c, d. While comparable  $X_0$  and  $X^-$  emission intensities are observed without applying the  $V_{\text{tip}}^{\text{DC}}$ , application of a positive  $V_{\text{tip}}^{\text{DC}}$  (+10 V) leads to a complete transition to the  $X_0$  dominant state. By contrast, application of a negative  $V_{\text{tip}}^{\text{DC}}$  (−10 V) results in a transition to the  $X^-$  dominant state, demonstrating electrical control of exciton-trion interconversion at the nanoscale region (Supplementary Fig. 11). We note that the PL spectra are fitted using Lorentz functions, with initial fitting parameters based on previous studies<sup>24,46,47</sup>. Furthermore, associated with the modification of  $X_0$  and  $X^-$  population, we observed a clear alteration of the PL intensity (Supplementary Fig. 12). The modified electron density significantly influences the recombination dynamics of  $X_0$  and  $X^-$  in the  $\text{MoS}_2$  ML, as previously observed through PL QY variations<sup>17,22</sup>.

### High-speed electrical modulation of exciton-trion interconversion

The nanoscale dimensions of the QNC allow for high-speed electrical modulation of exciton-trion interconversion. To deterministically modulate exciton or trion conversions, we superimpose an AC bias on the Au tip ( $V_{\text{tip}}^{\text{AC}}$ ) onto a DC offset, ensuring that the magnitude of the DC offset aligns with the amplitude of the  $V_{\text{tip}}^{\text{AC}}$ . Thus, the bidirectional



**Fig. 3 | Nanoscale exciton-trion interconversion through optical and electrical control.** **a** Contour plot of PL spectra of the MoS<sub>2</sub> ML as a function of the tip-sample distance. **b** Distance-dependent change of  $X_0$  (red) and  $X^-$  (blue) emission intensities, derived from (a). **c** PL spectra of the MoS<sub>2</sub> ML as a function of the  $V_{tip}^{DC}$ , when

the tip-sample distance is shorter than 3 nm (quantum tunneling regime). **d** Lorentz fitted PL spectra of the MoS<sub>2</sub> ML when the  $V_{tip}^{DC}$  is +10 V (top), 0 V (middle), and -10 V (bottom) on the Au tip. Black dashed lines in (a) and (c) indicate the energies of  $X_0$  and  $X^-$ .

modulation of  $X_0$  or  $X^-$  is enabled depending on the polarity of the DC offset, as shown in Fig. 4a. Figure 4b shows the second-order correlation function measured through the TCSPC module, with modulation frequencies varying from 0 MHz to 6.4 MHz while keeping the modulation amplitude on the Au tip to +5 V ( $X_0$  modulation). Specifically, the modulated PL signal undergoes splitting via a 50:50 multimode fiber optic coupler, with each portion individually measured by two APDs connected to the TCSPC module (Methods). This enables the analysis of high-speed exciton behaviors via PL, with a temporal resolution of  $\sim 350$  ps. The application of the positive DC offset stimulates the  $X_0$  conversion process, resulting in the enhanced PL QY (Supplementary Figs. 13, 14). Here, with the low excitation power of  $\sim 150$   $\mu$ W, we reveal that the modulation speed is limited to  $\sim 6.4$  MHz. To achieve higher modulation frequencies, overcoming the potential constraint posed by the retrapping of photo-excited holes at the metal-semiconductor interface is crucial, as the retrapping process reduces the recombination of photo-excited excitons until the trapped hole states are sufficiently occupied<sup>31</sup>. Indeed, with a finite number of trapped hole states, increasing the excitation power results in an elevated upper frequency limit, as it speeds up the retrapping process (Supplementary Fig. 15–17). Consequently, the increased coincidence is observed with the elevated modulation frequency of  $\sim 8$  MHz at the high excitation power of  $\sim 3.5$  mW. Upon applying the negative DC offset, it stimulates the  $X^-$  conversion process, reducing the PL QY of excitonic emission. This leads to the decreased coincidence with the modulation frequency of  $\sim 8$  MHz. Therefore, we achieve the maximum modulation frequency of  $\sim 8$  MHz for both exciton-to-trion and trion-to-exciton conversions, corresponding to a period  $\tau$  of  $\sim 125$  ns, as shown in Fig. 4c. The nanoscale metal-semiconductor interface induced by the QNC effectively facilitates the high-speed excitonic interconversion, as the trapped hole states are promptly occupied through its nanoscale dimension and the highly enhanced optical field.

## Discussion

In conclusion, our finding demonstrates the potential and versatility of the quantum tunneling nanoplasmonic cavity for observation of high-speed optoelectronic phenomena and their electrical modulation. Experimental investigations, including the nanoscale electrostatic doping and sub-diffraction-limited analysis of nano-optoelectronic

properties, provide comprehensive insights into nanoscale behaviors (Supplementary Figs. 18, 19 and Supplementary Note 1). Our study extends to the high-speed electrical modulation of excitonic quasiparticles, leading to the development of various nano-optoelectronic device platforms harnessing modified recombination dynamics<sup>17,48</sup>, nonlinearities<sup>49,50</sup>, valley polarizations<sup>15</sup>, and transport dynamics<sup>23,51</sup>. We achieve a remarkably high modulation frequency of  $\sim 8$  MHz and our findings suggest that the trapped hole states are possibly a key consideration for further improving modulation speed. The dependence on increasing excitation power should encounter limitations, notably when reaching a saturated density of excitons or causing a potential sample damage at high fluence level. While the elimination of the dielectric barrier effectively reduces the formation of trapped hole states, it may introduce the coupling with nonradiative higher-order plasmonic modes of metal, resulting in complete quenching of the photoluminescence<sup>52</sup>. Therefore, the concurrent development of optimized plasmonic structures<sup>53,54</sup> and the application of interface engineering techniques<sup>55,56</sup> will open a new avenue for achieving ultrafast nano-excitonic modulator.

## Methods

### Fabrication of high-k HfO<sub>2</sub> thin film on the Au substrate

The conventional cleaning treatment (acetone-methanol-IPA) was performed to remove impurities of the Si substrate, subsequently, a 50 nm-thick Au film was deposited on the substrate using an e-beam evaporator. Using the atomic layer deposition technique, we deposited a high-k HfO<sub>2</sub> thin film onto the Au film, employing Tetrakis (ethylmethylamino) hafnium as a precursor and H<sub>2</sub>O as a reactor at 280 °C in the N<sub>2</sub> atmosphere. The resulting film thickness was measured as 9.4 nm using UV-VIS ellipsometry. A 100 nm-thick Au bottom electrode layer was deposited onto the HfO<sub>2</sub> thin film using an e-beam evaporator, with a 5 nm-thick Cr layer used as an adhesive layer. The sample was coated with the epoxy resin (Norland Optical Adhesive NOA 61) for adhesion. The sample was then covered with a SiO<sub>2</sub> slide glass as the carrier substrate, and UV light was used to cure it. Subsequently, the Au layer was exfoliated from the Si template using tweezers and selectively removed with Au etchant. Our final step was to expose the Cr/Au layer as a bottom electrode with an area of 1 cm  $\times$  1 cm, by using an ion miller with a partially etched mask.



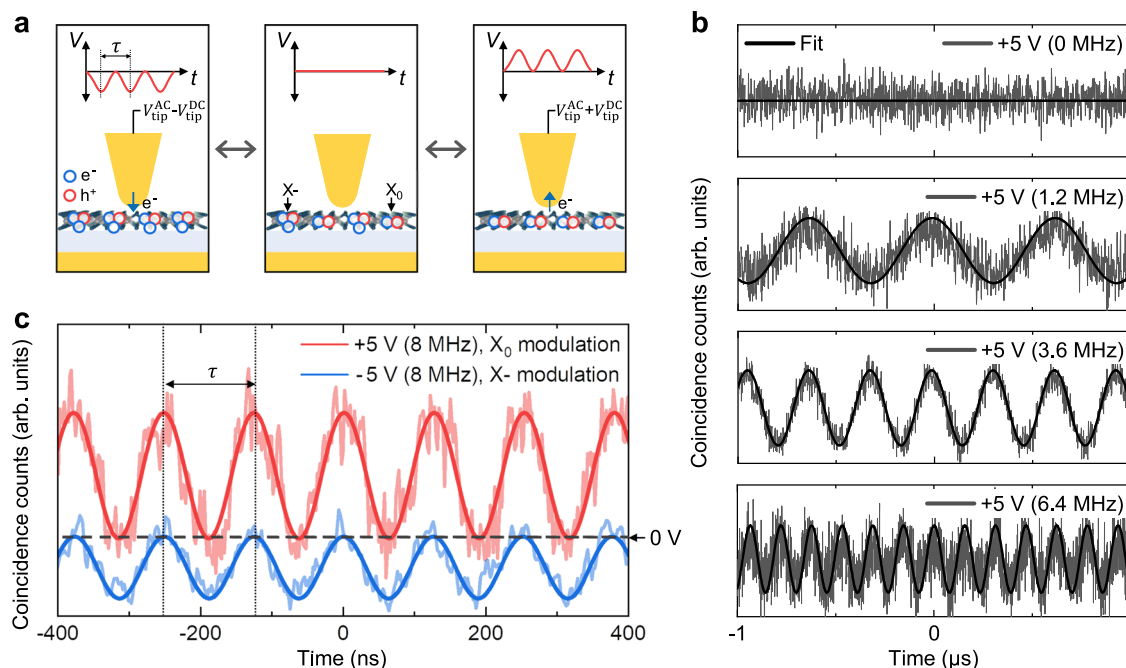


**Fig. 4 | Autocorrelation measurement of the high-speed electrical modulation of excitons and trions.** **a** Illustration depicting modified exciton behaviors in the MoS<sub>2</sub> ML with a different polarity of modulation amplitude. Left and right panels indicate the transition to X<sup>-</sup> dominant and X<sub>0</sub> dominant states, respectively. **b** Measured coincidence of the electrically modulated PL intensity for different

modulation frequencies, with the fixed amplitude of +5 V (X<sub>0</sub> modulation) and the excitation power of ~150 μW. **c** High-speed electrical modulation of X<sup>-</sup> conversion (−5 V, blue) and X<sub>0</sub> conversion (+5 V, red) with the excitation power of ~3.5 mW.  $\tau$  and  $V_{\text{tip}}^{\text{AC}}$  represent the period of excitonic modulation and the AC bias on the Au tip, respectively.

### Growth and transfer of MoS<sub>2</sub> monolayers

A two-zone furnace was used to grow the MoS<sub>2</sub> monolayer flakes; sulfur flakes (Merck, >99.99%) were placed in the upstream zone; a 0.01 M sodium molybdate aqueous solution was spun onto a SiO<sub>2</sub>/Si substrate as the molybdenum precursor; the substrate was loaded into the downstream zone; the sulfur flakes and substrate were heated at 200 °C and 750 °C temperatures, respectively, for 7 min and maintained for 8 min; the substrate was then cooled naturally to room temperature. The entire process was performed with an N<sub>2</sub> carrier gas at a flow rate of 600 SCCM. The as-grown MoS<sub>2</sub> was then coated with poly (methyl methacrylate) (PMMA) at 2500 rpm for 1 min. To delaminate the SiO<sub>2</sub>/Si substrate, the PMMA-coated sample was floated on a 2 M aqueous KOH solution. After delamination, the KOH residues were rinsed several times with deionized water. The PMMA/MoS<sub>2</sub> layer was scooped with the 10 nm thick HfO<sub>2</sub> layer on the Au substrate. Finally, the PMMA layer was removed using acetone and isopropyl alcohol.

### Quantum tunneling nanoplasmonic cavity

The MoS<sub>2</sub> monolayers were deposited onto the Au substrate with the 10 nm thick HfO<sub>2</sub> top layer, and they were mounted on a piezoelectric transducer (PZT, P-611.3X, Physik Instrumente) for precise XY scanning and atomic force feedback, achieving positioning precision of <0.1 nm. To enable the nanoplasmonic cavity, we utilized an Au tip with a radius of curvature of ~5–20 nm. This Au tip, created through an optimized electrochemical etching process, was affixed to a quartz tuning fork with a resonance frequency of 32.768 kHz. The distance between the tip and the sample was controlled using shear-force AFM and a digital AFM controller (R9+, RHK Technology). We combined a conventional optical spectroscopy setup with our home-built shear-force AFM system. To ensure a high-quality excitation beam, we introduced a diode laser with a wavelength of 594 nm. This laser was coupled to a single-mode optical fiber and subsequently collimated using an aspheric lens. The collimated laser beam was then passed

through a half-wave plate to align its polarization parallel to the tip's axis. Finally, the beam was focused onto the Au tip using a microscope objective (numerical aperture = 0.8, LMPLFLN100X, Olympus) with a side illumination configuration. To achieve precise laser coupling to the Au tip, we employed piezo actuators (9062-XYZ-PPP-M, Newport) to control the tip's position with an accuracy of ~30 nm. The collected optical responses were acquired using the same microscope objective in backscattering geometry. These responses were then filtered through an edge filter to eliminate the fundamental laser line. Subsequently, the optical signals were spectrally dispersed using a spectrometer (focal length = 328 mm, Kymera 328i, Andor) and recorded with a thermoelectrically cooled charge-coupled device (CCD, iDus 420, Andor) to generate the PL spectra. For the electric-field module to enable the quantum tunneling nanoplasmonic cavity, the tip and sample were electrically connected to a function generator. By applying a potential difference between the tip and sample, a localized electric field was induced between the tip and sample. To read the tunneling current, we used the STM module (R9+, RHK Technology).

### Autocorrelation measurement setup

To measure the second-order correlation function of the electrically modulated exciton-trion interconversion and correspondingly modified PL quantum yield, the He-Ne laser with a wavelength of 594 nm was employed to continuously excite the MoS<sub>2</sub> monolayer. Subsequently, the PL signal was split by the 50:50 multimode fiber optic coupler (TM50R5F1A, Thorlabs) and collected by two separately located avalanche photodetectors (Si-APD, SPCM-AQRH-14-FC, Excelitas Technologies). APDs were connected to a time-correlated single photon counting (TCSPC, quTAG-MC, quTools GmbH) to calculate the time correlation.

### Data availability

Relevant data supporting the key findings of this study are available within the article and the Supplementary Information file. All raw data

generated during the current study are available from the corresponding authors upon request.

## References

- Regan, E. C. et al. Emerging exciton physics in transition metal dichalcogenide heterobilayers. *Nat. Rev. Mater.* **7**, 778–795 (2022).
- Lopez-Sanchez, O., Lembke, D., Kayci, M., Radenovic, A. & Kis, A. Ultrasensitive photodetectors based on monolayer MoS<sub>2</sub>. *Nat. Nanotechnol.* **8**, 497–501 (2013).
- Ross, J. S. et al. Electrically tunable excitonic light-emitting diodes based on monolayer WSe<sub>2</sub> p–n junctions. *Nat. Nanotechnol.* **9**, 268–272 (2014).
- Ye, Y. et al. Monolayer excitonic laser. *Nat. Photon.* **9**, 733–737 (2015).
- Sung, J. et al. Room-temperature continuous-wave indirect-bandgap transition lasing in an ultra-thin WS<sub>2</sub> disk. *Nat. Photon.* **16**, 792–797 (2022).
- Bernardi, M., Palummo, M. & Grossman, J. C. Extraordinary sunlight absorption and one nanometer thick photovoltaics using two-dimensional monolayer materials. *Nano Lett.* **13**, 3664–3670 (2013).
- Combescot, M., Betbeder-Matibet, O. & Combescot, R. Bose–Einstein condensation in semiconductors: the key role of dark excitons. *Phys. Rev. Lett.* **99**, 176403 (2007).
- Poem, E. et al. Accessing the dark exciton with light. *Nat. Phys.* **6**, 993–997 (2010).
- Combescot, M., Combescot, R. & Dubin, F. Bose–Einstein condensation and indirect excitons: a review. *Rep. Prog. Phys.* **80**, 066501 (2017).
- Tonndorf, P. et al. Single-photon emission from localized excitons in an atomically thin semiconductor. *Optica* **2**, 347–352 (2015).
- He, Y.-M. et al. Single quantum emitters in monolayer semiconductors. *Nat. Nanotechnol.* **10**, 497–502 (2015).
- Srivastava, A. et al. Optically active quantum dots in monolayer WSe<sub>2</sub>. *Nat. Nanotechnol.* **10**, 491–496 (2015).
- Jauregui, L. A. et al. Electrical control of interlayer exciton dynamics in atomically thin heterostructures. *Science* **366**, 870–875 (2019).
- Cheng, G., Li, B., Jin, Z., Zhang, M. & Wang, J. Observation of diffusion and drift of the negative trions in monolayer WS<sub>2</sub>. *Nano Lett.* **21**, 6314–6320 (2021).
- Zhang, Q. et al. Prolonging valley polarization lifetime through gate-controlled exciton-to-trion conversion in monolayer molybdenum ditelluride. *Nat. Commun.* **13**, 4101 (2022).
- Singh, A. et al. Long-lived valley polarization of intravalley trions in monolayer WSe<sub>2</sub>. *Phys. Rev. Lett.* **117**, 257402 (2016).
- Amani, M. et al. Near-unity photoluminescence quantum yield in MoS<sub>2</sub>. *Science* **350**, 1065–1068 (2015).
- Das, S., Kallatt, S., Abraham, N. & Majumdar, K. Gate-tunable trion switch for excitonic device applications. *Phys. Rev. B* **101**, 081413 (2020).
- Lin, J. D. et al. Electron-doping-enhanced trion formation in monolayer molybdenum disulfide functionalized with cesium carbonate. *ACS Nano* **8**, 5323–5329 (2014).
- Harats, M. G., Kirchhof, J. N., Qiao, M., Greben, K. & Bolotin, K. I. Dynamics and efficient conversion of excitons to trions in non-uniformly strained monolayer WS<sub>2</sub>. *Nat. Photon.* **14**, 324–329 (2020).
- Wang, Z. et al. Greatly enhanced resonant exciton-trion conversion in electrically modulated atomically thin WS<sub>2</sub> at room temperature. *Adv. Mater.* **35**, 2302248 (2023).
- Lien, D.-H. et al. Electrical suppression of all nonradiative recombination pathways in monolayer semiconductors. *Science* **364**, 468–471 (2019).
- Uddin, S. Z. et al. Neutral exciton diffusion in monolayer MoS<sub>2</sub>. *ACS Nano* **14**, 13433–13440 (2020).
- Mouri, S., Miyauchi, Y. & Matsuda, K. Tunable photoluminescence of monolayer MoS<sub>2</sub> via chemical doping. *Nano Lett.* **13**, 5944–5948 (2013).
- Wang, X. et al. Photoinduced doping and photoluminescence signature in an exfoliated WS<sub>2</sub> monolayer semiconductor. *RSC Adv.* **6**, 27677–27681 (2016).
- Lee, H. et al. All-optical control of high-purity trions in nanoscale waveguide. *Nat. Commun.* **14**, 1891 (2023).
- Lee, H. et al. Electrically tunable single polaritonic quantum dot at room temperature. *Phys. Rev. Lett.* **132**, 133001 (2024).
- Allain, A., Kang, J., Banerjee, K. & Kis, A. Electrical contacts to two-dimensional semiconductors. *Nat. Mater.* **14**, 1195–1205 (2015).
- Carozo, V. et al. Optical identification of sulfur vacancies: Bound excitons at the edges of monolayer tungsten disulfide. *Sci. Adv.* **3**, e1602813 (2017).
- Cui, Q. et al. Robust and high photoluminescence in WS<sub>2</sub> monolayer through in situ defect engineering. *Adv. Func. Mater.* **31**, 2105339 (2021).
- Zhu, G. et al. Room-temperature high-speed electrical modulation of excitonic distribution in a monolayer semiconductor. *Nat. Commun.* **14**, 6701 (2023).
- Tran, M. D. et al. Role of hole trap sites in MoS<sub>2</sub> for inconsistency in optical and electrical phenomena. *ACS Appl. Mater. Interfaces* **10**, 10580–10586 (2018).
- Furchi, M. M., Polyushkin, D. K., Pospischil, A. & Mueller, T. Mechanisms of photoconductivity in atomically thin MoS<sub>2</sub>. *Nano Lett.* **14**, 6165–6170 (2014).
- Valsaraj, A., Chang, J., Rai, A., Register, L. F. & Banerjee, S. K. Theoretical and experimental investigation of vacancy-based doping of monolayer MoS<sub>2</sub> on oxide. *2D Mater.* **2**, 045009 (2015).
- Guha, S. & Narayanan, V. Oxygen vacancies in high dielectric constant oxide-semiconductor films. *Phys. Rev. Lett.* **98**, 196101 (2007).
- Lee, H. et al. Tip-induced strain engineering of a single metal halide perovskite quantum dot. *ACS Nano* **15**, 9057–9064 (2021).
- Lee, H. et al. Drift-dominant exciton funneling and trion conversion in 2D semiconductors on the nanogap. *Sci. Adv.* **8**, eabm5236 (2022).
- Koo, Y. et al. Dynamical control of nanoscale light-matter interactions in low-dimensional quantum materials. *Light Sci. Appl.* **13**, 30 (2024).
- Mohamed, M. B., Volkov, V., Link, S. & El-Sayed, M. A. The lightning gold nanorods: fluorescence enhancement of over a million compared to the gold metal. *Chem. Phys. Lett.* **317**, 517–523 (2000).
- Lee, H. et al. Tip-enhanced photoluminescence nano-spectroscopy and nano-imaging. *Nanophotonics* **9**, 3089–3110 (2020).
- Knight, M. W., Wu, Y., Lassiter, J. B., Nordlander, P. & Halas, N. J. Substrates matter: influence of an adjacent dielectric on an individual plasmonic nanoparticle. *Nano Lett.* **9**, 2188–2192 (2009).
- Rycenga, M. et al. Generation of hot spots with silver nanocubes for single-molecule detection by surface-enhanced Raman scattering. *Angew. Chem. Int. Ed.* **50**, 5473 (2011).
- Wang, S.-Y. et al. Reactive ion etching-assisted surface-enhanced Raman scattering measurements on the single nanoparticle level. *Appl. Phys. Lett.* **104** (2014).
- Ross, J. S. et al. Electrical control of neutral and charged excitons in a monolayer semiconductor. *Nat. Commun.* **4**, 1474 (2013).
- Clavero, C. Plasmon-induced hot-electron generation at nanoparticle/metal-oxide interfaces for photovoltaic and photocatalytic devices. *Nat. Photon.* **8**, 95–103 (2014).
- Hejazi, D. et al. MoS<sub>2</sub> nanosheets with narrowest excitonic line widths grown by flow-less direct heating of bulk powders: Implications for sensing and detection. *ACS Appl. Nano Mater.* **4**, 2583–2593 (2021).
- Neumann, A. et al. Opto-valleytronic imaging of atomically thin semiconductors. *Nat. Nanotechnol.* **12**, 329–334 (2017).

48. Li, Q. et al. A purcell-enabled monolayer semiconductor free-space optical modulator. *Nat. Photon.* **17**, 897–903 (2023).
49. Seyler, K. L. et al. Electrical control of second-harmonic generation in a WSe<sub>2</sub> monolayer transistor. *Nat. Nanotechnol.* **10**, 407–411 (2015).
50. Emmanuele, R. et al. Highly nonlinear trion-polaritons in a monolayer semiconductor. *Nat. Commun.* **11**, 3589 (2020).
51. Kato, T. & Kaneko, T. Transport dynamics of neutral excitons and trions in monolayer WS<sub>2</sub>. *ACS Nano* **10**, 9687–9694 (2016).
52. Anger, P., Bharadwaj, P. & Novotny, L. Enhancement and quenching of single-molecule fluorescence. *Phys. Rev. Lett.* **96**, 113002 (2006).
53. Rogobete, L., Kaminski, F., Agio, M. & Sandoghdar, V. Design of plasmonic nanoantennae for enhancing spontaneous emission. *Opt. Lett.* **32**, 1623–1625 (2007).
54. Chen, X.-W., Agio, M. & Sandoghdar, V. Metallo-dielectric hybrid antennas for ultrastrong enhancement of spontaneous emission. *Phys. Rev. Lett.* **108**, 233001 (2012).
55. Zou, X. et al. Interface engineering for high-performance top-gated MoS<sub>2</sub> field-effect transistors. *Adv. Mater.* **26**, 6255–6261 (2014).
56. Liu, Y. et al. Approaching the Schottky–Mott limit in van der Waals metal–semiconductor junctions. *Nature* **557**, 696–700 (2018).

## Acknowledgements

This work was supported by the National Research Foundation of Korea (NRF) grants (2020R1C1C1011301, 2022M3H4A1A0409639612, RS-2023-00254055, 2021R1A6A1A1004294413), the Samsung Science and Technology Foundation (SSTP-BA2102-05), and the MSIT (Ministry of Science and ICT) under the ITRC (Information Technology Research Center) support program (IITP-2022-RS-2022-00164799). K.K.K. acknowledges support from the Basic Science Research (2022R1A2C2091475) through the National Research Foundation of Korea (NRF). H.-R.P. acknowledges NRF-RS-2024-00353252. V.K. acknowledges support by Priority 2030 Federal Academic Leadership Program.

## Author contributions

H.L., S.K., K.-D.P. conceived the experiments. H.L., S.K. designed quantum tunneling nanoplasmonic cavity. S.K., H.L. performed optical and electrical measurement. S.E., G.J., H.-R.P. optimized and prepared the substrates. H.L., H.J., V.K. performed the theoretical calculations. H.L., S.K., J.B. conducted TCSPC measurement. S.H.C., K.K.K. prepared and transferred MoS<sub>2</sub> ML onto the device. S.K., H.L., K.-D.P. analyzed the

data, and all authors discussed the results. H.L., S.K., K.-D.P. wrote the manuscript with contributions from all authors. K.-D.P. supervised the project.

## Competing interests

The authors declare no competing interests.

## Additional information

**Supplementary information** The online version contains supplementary material available at <https://doi.org/10.1038/s41467-024-52813-5>.

**Correspondence** and requests for materials should be addressed to Kyoung-Duck Park.

**Peer review information** *Nature Communications* thanks Shuai Zhang and the other, anonymous, reviewers for their contribution to the peer review of this work. A peer review file is available.

**Reprints and permissions information** is available at <http://www.nature.com/reprints>

**Publisher's note** Springer Nature remains neutral with regard to jurisdictional claims in published maps and institutional affiliations.

**Open Access** This article is licensed under a Creative Commons Attribution-NonCommercial-NoDerivatives 4.0 International License, which permits any non-commercial use, sharing, distribution and reproduction in any medium or format, as long as you give appropriate credit to the original author(s) and the source, provide a link to the Creative Commons licence, and indicate if you modified the licensed material. You do not have permission under this licence to share adapted material derived from this article or parts of it. The images or other third party material in this article are included in the article's Creative Commons licence, unless indicated otherwise in a credit line to the material. If material is not included in the article's Creative Commons licence and your intended use is not permitted by statutory regulation or exceeds the permitted use, you will need to obtain permission directly from the copyright holder. To view a copy of this licence, visit <http://creativecommons.org/licenses/by-nc-nd/4.0/>.

© The Author(s) 2024